RSC Advances

PAPER

View Article Online
View Journal | View Issue

Cite this: *RSC Adv.*, 2026, **16**, 12092

Sm^{2+} doped strontium pentaborate chloride for dual-modal temperature imaging

Zhongmin Cao,[a] Zhicheng Liao,[b] Qian Zhang,[b] Li Li,[a] Xianju Zhou,[a] Sha Jiang,[a] Guangxin Xie,[a] Yonghu Chen,[b] Min Yin[b] and Xiantao Wei*[b]

A multimodal thermometry material, Sm^{2+} doped $Sr_2B_5O_9Cl$, was successfully synthesized and investigated for its potential in thermometry and temperature imaging. The temperature-dependent behaviors of the fluorescence intensity ratio (FIR), decay lifetime, dual-light-path intensity ratio (DLIR) and time-resolved intensity ratio (TRIR) were systematically studied, revealing high temperature sensitivity for each strategy. To facilitate temperature imaging, charge-coupled device (CCD) cameras were employed instead of conventional spectrometers to record the spatial distribution of fluorescence intensity and establish calibration curves correlating temperature. Temperature distribution imaging on printed circuit boards was successfully demonstrated using both the DLIR method and the TRIR technique. The results indicate that the developed material exhibits excellent performance for both thermometric sensing and temperature imaging applications.

Received 12th December 2025
Accepted 25th February 2026

DOI: 10.1039/d5ra09629d

rsc.li/rsc-advances

Introduction

Temperature is one of the most important physical parameters. Its precise measurement is of great significance for scientific research and industrial production. With the fast development of science and technology, the working conditions for temperature measurement that researchers face nowadays are becoming increasingly complex. Traditional contact thermometry, which relies on physical probes, is often unsuitable for extremely harsh, miniaturized, or fragile targets. Moreover, a growing number of applications—from analysing thermal management in microchips[1–4] to monitoring physiological processes in biological tissues[5–7]—demand the acquisition of two- or even three-dimensional temperature maps to fully elucidate underlying mechanisms. For these scenarios, traditional point-measurement techniques are fundamentally inadequate, as mapping temperature distributions through sequential point-by-point detection is prohibitively time-consuming and incapable of capturing dynamic thermal events in real-time.

Luminescence-based optical thermometry has emerged as a powerful solution to these challenges, enabling non-contact measurement and real-time visualization of temperature distributions. This technique leverages the temperature-dependent characteristics of luminescent materials, offering distinct advantages including remote detection capability, rapid response, high sensitivity, and inherent spatial resolution. Consequently, it has garnered significant research interest, leading to the development of diverse material systems such as rare-earth-doped probes,[8–11] transition-metal-ion-activated probes,[12–14] and quantum dots.[15,16] Among these various luminescent probes, those based on rare-earth (RE) ions stand out due to their exceptional sensitivity, outstanding thermal and chemical stability, and remarkable resistance to environmental interference. These attributes make RE-doped materials particularly well-suited for reliable temperature imaging, even under complex and demanding operational conditions.

In RE-doped probes, the trivalent or divalent RE ions serve as the luminescent centres. Several of their emission characteristics exhibit strong temperature dependence, providing the foundation for various thermometric approaches. These include the fluorescence intensity ratio (FIR) between two thermally coupled levels,[17–19] the decay lifetime of an excited state,[19–21] the absolute emission intensity,[1,4] and shifts in the emission peak wavelength. Notably, the FIR and decay lifetime techniques are considered more robust for practical applications because they are largely immune to fluctuations in excitation intensity and light path loss, which has made them the focus of extensive research using conventional spectroscopic point-detection methods.

The transition from point sensing to real-time temperature distribution imaging necessitates new measurement strategies and instrumentation. Charge-coupled device (CCD) cameras are ideally suited for this task, as they can simultaneously capture intensity information from every spatial point within a target area in a single exposure. Leveraging this capability, two primary imaging techniques have been developed for RE-based

[a]*College of Science, Chongqing University of Posts and Telecommunications, Chongqing 400065, P. R. China*

[b]*School of Physical Sciences, University of Science and Technology of China, Hefei, Anhui 230026, P. R. China. E-mail: wxt@ustc.edu.cn*

thermometry: the dual-light-path intensity ratio (DLIR) method[22] and the time-resolved intensity ratio (TRIR) method.[1–4] These techniques are the spatial imaging counterparts to the traditional FIR and decay lifetime measurements, respectively. The DLIR method employs two cameras equipped with specific optical filters to capture intensities across two distinct wavelength regions, thereby obtaining the intensity ratio for each pixel. While the TRIR method extracts the integrated intensities over two predefined time intervals following the cessation of excitation using a single ICCD camera, and examines the temperature dependence of the intensity ratio, which is intrinsically linked to the fluorescence decay lifetime. The dual-light-path method is most effective for materials exhibiting well-separated emission bands, facilitating straightforward calculation of the intensity ratio. In contrast, the time-resolved method is preferred for materials whose decay lifetime shows pronounced temperature sensitivity.

The Sm^{2+} ion is particularly renowned for its exceptional temperature sensitivity in both FIR- and lifetime-based sensing schemes.[4,22] This unique property, observed in hosts like SrB_4O_7 and $M_2B_5O_9Cl$ (M = Ba, Sr),[23,24] originates from thermal coupling effect between the $4f^6$ and $4f5d^1$ energy levels. Remarkably, this coupling remains effective even when the energy gap exceeds 2000 cm^{-1}, allowing the FIR technique to circumvent the sensitivity limitations imposed by the traditional thermal coupling rules that govern transitions within the 4f configuration. Furthermore, the $4f^55d^1 \rightarrow 4f^6$ transition is parity-allowed, resulting in a decay lifetime on the order of microseconds. As temperature increases, an increasing fraction of the excited Sm^{2+} ions decay through this fast channel, causing the average measured lifetime to shift dramatically from the millisecond range (characteristic of the forbidden 4f–4f transitions) to the microsecond range. This can lead to a reduction in lifetime by several orders of magnitude, providing a very sensitive thermometric parameter. These combined attributes make Sm^{2+} an exceptionally promising candidate for high-performance temperature imaging.

Among Sm^{2+} doped materials, SrB_4O_7: Sm^{2+} has been extensively characterized for thermometry, using both traditional[19] and CCD-based techniques.[4,22] While it demonstrates outstanding performance, its practical application is constrained by a relatively high operational temperature threshold; the 5d–4f transition only becomes significant above approximately 373 K. This high activation temperature limits its suitability for emerging fields such as microelectronics and bioscience, where operation near room temperature is often essential. Consequently, identifying a host lattice that enables the 5d–4f transition of Sm^{2+} at lower temperatures is critical for advancing Sm^{2+} based temperature imaging. The chloroborate compound $Sr_2B_5O_9Cl$ has been identified as such a promising host, reported to facilitate this transition at a lower temperature. Additionally, the synthesis of chloroborates (*e.g.*, $Sr_2B_5O_9Cl$, $Ba_2B_5O_9Cl$) is generally more facile compared to their borate analogues (*e.g.*, CaB_4O_7, BaB_4O_7). Given these advantages—a lower operational temperature range and straightforward synthesis—$Sr_2B_5O_9Cl$ was selected as the host material for this in-depth investigation into the temperature imaging potential of Sm^{2+}.

In this work, we present a comprehensive study on Sm^{2+} doped $Sr_2B_5O_9Cl$, systematically evaluating its potential as a versatile optical thermometric material. We investigate its temperature-dependent properties using four distinct methods: the fluorescence intensity ratio (FIR), decay lifetime, dual-light-path FIR, and time-resolved intensity ratio. Our results demonstrate that this material exhibits excellent sensitivity across all modalities, strong emission signal, and a favourably lower operating temperature range. These combined attributes establish $Sr_2B_5O_9Cl$: Sm^{2+} as a highly promising candidate for multi-mode temperature sensing and imaging applications.

Experimental

The Sm^{2+} doped $Sr_2B_5O_9Cl$ sample was synthesized *via* a conventional high-temperature solid–state reaction method. All starting materials, including strontium carbonate ($SrCO_3$), strontium chloride ($SrCl_2$), boric acid (H_3BO_3), and samarium oxide (Sm_2O_3), were of analytical grade and used without further purification. These reagents were weighed according to the predetermined stoichiometric ratio, thoroughly mixed, and ground in an agate mortar. The mixture was then preheated at 500 °C for 1 hour in a muffle furnace. Subsequently, the resulting precursor was fully reground and sintered at 850 °C for 4 hours under a reducing atmosphere (*e.g.*, flowing N_2/H_2 mixture or active carbon embedding) to facilitate the reduction of Sm^{3+} to Sm^{2+} and obtain the final crystalline product.

The crystal structures of the synthesized samples were determined by X-ray diffraction (XRD) (Rigaku-TTR-III) with Cu Kα radiation (λ = 0.154 18 nm) in the 2θ range from 10° to 80°. Photoluminescence emission spectra were recorded using an Omni-λ5028i monochromator and a charge-coupled device (Andor DU401ABVF). The excitation source was an Opolette 355 LD laser, the output wavelength we used was 355 nm with a pulse duration of 7 ns and a pulse repetition rate of 20 Hz. The decay curves were recorded with the help of a Tektronix TDS2024 digital storage oscilloscope. The powder sample was pressed onto a heating stage to form a thin layer for measurement of time resolved intensity ratio in the temperature range of 333–533 K. The temperature of the sample was controlled by a Laker Shore Model 336 temperature controller with closed cycle cryocoolers (Advanced Research Systems, DE-202AI). The temperature imaging system is built on a fluorescent microscope and the fluorescence images under the excitation of 355 nm pulsed laser are captured by an ICCD (Andor iStar 340 T 18U73) with active pixels of 1330 × 512, effective pixel size of 13.5 × 13.5 μm and minimum optical gate width of 2 ns.

Results and discussion

Structure and morphology

The phase purity and crystal structure of the as-synthesized $Sr_2B_5O_9Cl$: Sm^{2+} sample were examined by XRD. Fig. 1 presents the XRD pattern of the sample alongside the standard pattern for pure $Sr_2B_5O_9Cl$ (JCPDS No. 27-890). All the observed

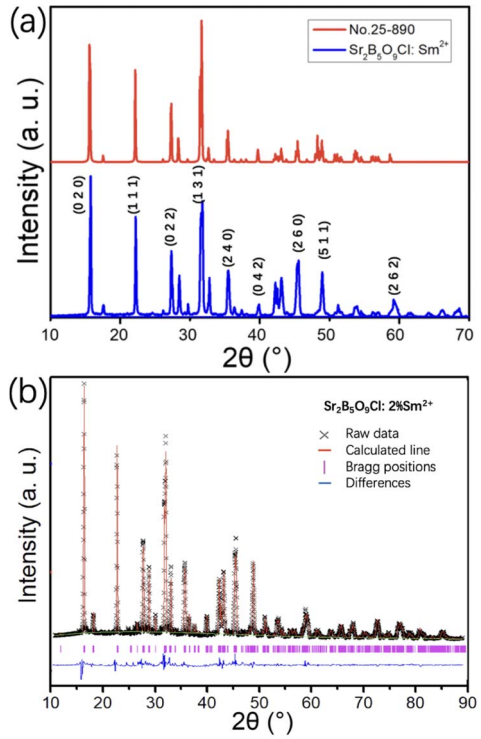

Fig. 1 (a) XRD pattern of the $Sr_2B_5O_9Cl$: 2%Sm^{2+} and the No. 23-890 standard card, (b) Rietveld refined XRD diffractograms of the $Sr_2B_5O_9Cl$: 2%Sm^{2+} sample.

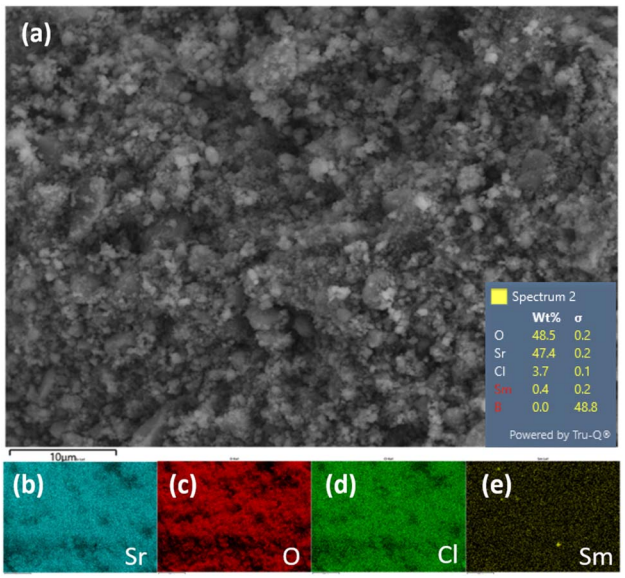

Fig. 2 (a) SEM image and (b–e) EDS elemental mapping of the $Sr_2B_5O_9Cl$: 2%Sm^{2+}.

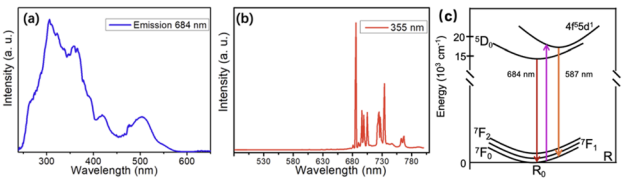

Fig. 3 (a) Excitation spectra of $Sr_2B_5O_9Cl$: 2%Sm^{2+} monitoring 685 nm emission; (b) emission spectra of $Sr_2B_5O_9Cl$: 2%Sm^{2+} excited by 355 nm laser; (c) schematic energy level diagram of the Sm^{2+} ions in $Sr_2B_5O_9Cl$.

diffraction peaks can be well indexed to the standard pattern, confirming the successful formation of a pure phase with high crystallinity. A slight shift of the diffraction peaks to lower angles is observed, which is attributable to the successful incorporation of Sm^{2+} ions into the $Sr_2B_5O_9Cl$ host lattice, since the ionic radius of Sm^{2+} is larger than that of Sr^{2+}.

The initial model for refinement was based on the known structure of $Sr_2B_5O_9Cl$. The reliability factors $R_p = 5.23\%$ and $R_{wp} = 7.16\%$ obtained for the material indicate that the refined results are reliable. The unit cell parameters were determined to be $a = 11.318$ Å, $b = 11.387$ Å, $c = 6.496$ Å, with $\alpha = \beta = \gamma = 90°$, corresponding to an orthorhombic system. The unit cell volume is 837.25 Å^3.

The Scanning Electron Microscope (SEM) of the sample is shown in Fig. 2(a). It is obtained from the SEM photo that the sample consists of particles around 1 μm that agglomerated together. Through the Energy Dispersive Spectrometer (EDS) in Fig. 2(b–e) we can learn that the Sm, Sr and other elements are evenly distributed in the sample.

Photoluminescence properties

The excitation and emission spectrum of the sample at room temperature are measured to study the sample's luminescence properties (Fig. 3). The $Sr_2B_5O_9Cl$: 2%Sm^{2+} is chosen due to its strong luminescence intensity and emission from a single site (Fig. S1). The emission spectrum (Fig. 3(a)) shows that at room temperature the sample only shows transitions that originate from 4f energy level. The strongest luminescence peak located at 685 nm is designated as $^5D_0$ to $^7F_0$. The peaks at the long wavelengths originates from $^5D_0$ to $^7F_1$ and $^7F_2$. The excitation spectrum (Fig. 3(b)) was monitored at the emission wavelength of 685 nm. There are several excitation bands and the best two excitation bands are around 306 nm and 356 nm. Thus, it is reasonable to choose 355 nm as the excitation wavelength.

The room-temperature photoluminescence (PL) properties of $Sr_2B_5O_9Cl$: 2%Sm^{2+} are presented in Fig. 3. The emission spectrum (Fig. 3(a)), obtained under excitation at 356 nm, is dominated by sharp lines characteristic of 4f–4f intra-configurational transitions of Sm^{2+}. The most intense peak at 685 nm is assigned to the $^5D_0$ to $^7F_0$ transition. The weaker features at longer wavelengths originate from the $^5D_0$ to $^7F_1$ and $^5D_0$ to $^7F_2$ transitions. The excitation spectrum (Fig. 3(b)), monitored at the 685 nm emission, reveals several broad bands. The two most prominent bands, centered at approximately 306 nm and 356 nm, are attributed to 4f to 5d transitions of Sm^{2+}. Based on these findings, an excitation wavelength of 355 nm was selected for all subsequent measurements, as it efficiently populates the emitting states.

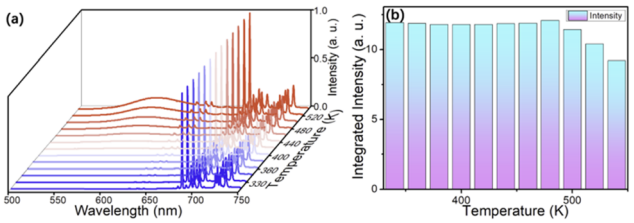

Fig. 4 Temperature dependent emission spectra (a) and integrated intensity (b).

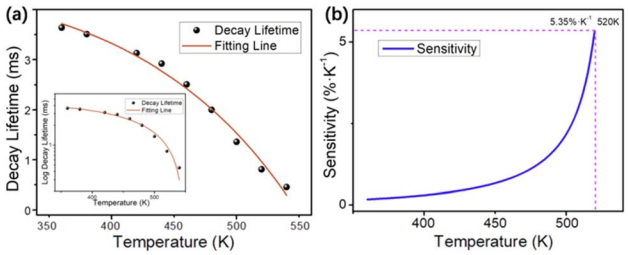

Fig. 6 (a) Temperature dependent decay lifetime and its fitting line; (b) relative sensitivity of the temperature dependent decay lifetime.

Temperature-dependent intensity ratio

The temperature-dependent photoluminescence (PL) spectra and decay lifetimes of $Sr_2B_5O_9Cl$: Sm^{2+} were systematically investigated to evaluate its thermometric performance. Fig. 4(a) displays the temperature-dependent PL spectra, normalized to the 685 nm peak of Sm^{2+}. As temperature increases, a distinct broad emission band emerges in the range of 500–675 nm, with a maximum around 587 nm. This band is attributed to the $4f^55d^1$ to $4f^6$ transition of Sm^{2+}, which becomes progressively more intense relative to the sharp 4f–4f lines at higher temperatures due to the thermal population of the 5d excited state. According to the excitation spectra and emission spectra at high temperatures, the stokes shift of 5d energy levels are calculated to be 2766.2 cm^{-1}.

The temperature dependence of the total integrated PL intensity is plotted in Fig. 4(b). Notably, the material exhibits exceptional thermal stability, with negligible thermal quenching observed below 500 K. Above this temperature, the intensity only undergoes a gradual decrease. This remarkable resistance to thermal quenching is a significant advantage for high-temperature thermometry applications, as it ensures a strong signal throughout the operational range.

The temperature-dependent fluorescence intensity ratio (FIR) was defined as the integrated intensity of the 5d-band (500–587 nm) divided by that of the 4f-band (680–750 nm). The integration range for the 5d-band was carefully selected to avoid potential overlap with the $^5D_0$ to $^7F_0$ transitions around 630 nm. The resulting FIR as a function of temperature is presented in Fig. 5 (a), along with a fitting curve. The data were well-described by the following Boltzmann-type equation:

$$R = Be^{-\frac{\Delta E}{k_B T}} \quad (1)$$

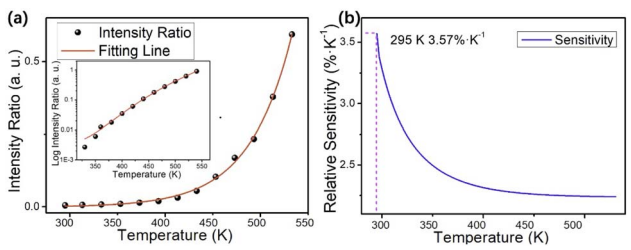

Fig. 5 (a) Temperature dependent intensity ratio and its fitting result; (b) relative sensitivity of the temperature dependent intensity ration.

with parameters $\Delta E = 3586.8$ cm^{-1} and $B = 12\,932$. The overall agreement between the fit and the experimental data is good, as further visualized in the inset of Fig. 5(a), which plots the FIR on a logarithmic scale to better assess the low-temperature region. A noticeable deviation between the fit and the experimental data is observed below 350 K, which can be attributed to the extremely weak intensity of the 5d-band emission at these temperatures. As the temperature increases, the intensity of the 5d emission rises. However, due to its broad-band nature, the emission intensity at each specific wavelength remains significantly weaker than the sharp line emission observed at lower temperatures, resulting in a reduced signal-to-noise ratio for the derived FIR values.

The relative sensitivity (S_R) for the FIR method was calculated and is depicted in Fig. 5(b). A maximum S_R of 3.57% K^{-1} is achieved at 300 K. It should be noted that the sensitivity values at the lowest temperatures (where data fitting is less reliable due to low signal-to-noise ratio) should be interpreted with caution. Nevertheless, across the majority of the investigated temperature range, S_R remains above 2.24% K^{-1}, demonstrating a sensitivity that is highly competitive for practical temperature sensing applications.

The temperature dependence of the decay lifetime, monitored at the 685 nm emission ($^5D_0$ to $^7F_0$), is presented in Fig. 6(a). The lifetime undergoes a rapid decrease with increasing temperature. This dramatic reduction is a direct consequence of the thermal population of the 5d levels, which provides a fast, parity-allowed radiative decay pathway ($4f^55d^1 \rightarrow 4f^6$) that effectively shortens the measured lifetime

Table 1 Relative sensitivity information of recently reported work[a]

Materials	Mode	Temperature (S_R Max)	Max S_R (% K^{-1})	Ref.
SrB_4O_7: Sm^{2+}	FIR	720 K	3.52	19
BaFCl: 1%Sm^{2+}	DL	775 K	2.40	25
SrFBr: 1%Sm^{2+}	DL	700 K	3.40	25
BaFBr: 1%Sm^{2+}	DL	123 K	1.30	25
ScF_3: Yb^{3+}/Tm^{3+}	LIR	523 K	1.60	26
$Ba_3(VO_4)_2$: Eu^{3+}	LIR	773 K	2.01	27
$Sr_2B_5O_9Cl$: Sm^{2+}	FIR	295 K	3.57	This work
$Sr_2B_5O_9Cl$: Sm^{2+}	DL	520 K	5.35	This work

[a] FIR stands for fluorescence intensity ratio; DL stands for decay lifetime.

compared to the forbidden 4f–4f transitions. The experimental data are accurately fitted by the following equation:

$$\tau = 0.0042 - 0.0002e^{\frac{-T}{85.7}} \quad (2)$$

The corresponding relative sensitivity, plotted in Fig. 6(b), exhibits a monotonic increase with temperature, reaching a notably high value of 5.35% K^{-1} at 520 K.

The above results confirm that both the FIR and decay lifetime methods in $Sr_2B_5O_9Cl$: Sm^{2+} yield excellent relative sensitivities. Motivated by these promising point-sensing characteristics, we proceeded to evaluate its performance for temperature distribution imaging, implementing both CCD camera-based FIR and time-resolved intensity ratio techniques (Table 1).

FIR based temperature imaging with a CCD camera

To achieve real-time temperature imaging *via* the FIR technique, a dual-light-path optical system integrated with two CCD cameras was implemented, following the approach described in our prior work.[22] This configuration simultaneously captures fluorescence intensities within two separate spectral bands: one corresponding to the 5d to 4f emission (500–580 nm) and the other to the 4f–4f emission (680–750 nm). Long-pass and short-pass filters were respectively incorporated into each optical path to ensure effective spectral isolation.

During data acquisition, two spatially co-registered images are captured: one ($Image_{5d}$) representing the intensity distribution in the 5d-band (500–580 nm) and the other ($Image_{4f}$) for the 4f-band (680–750 nm). The FIR distribution map is then computed on a pixel-by-pixel basis by taking the ratio $Image_{5d}/Image_{4f}$. This entire process, from image capture to FIR map generation, can be completed in less than 0.5 seconds, thereby enabling rapid, real-time temperature imaging.

For calibration, the sample was heated to a series of known temperatures, and the corresponding average FIR value from the imaging area was recorded to establish the FIR-temperature relationship (Fig. 7(a)). Once this calibration curve was obtained, the temperature distribution of any object coated with the sample could be determined in real-time by acquiring a new image pair and converting the FIR map into a temperature map using the calibration function.

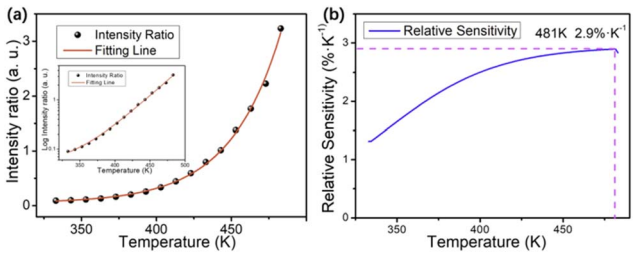

Fig. 7 (a) The fitting result of the temperature dependent intensity ratio based on dual light path system; (b) relative sensitivity of intensity ratio based on dual light path system.

The calibration data for $Sr_2B_5O_9Cl$: Sm^{2+}, acquired in the range of 333 K to 483 K, is presented in Fig. 7(a). The superior light-collecting efficiency of the CCD camera enabled reliable FIR measurements to be extended to lower temperatures compared to spectrometer-based detection. The data were fitted with a sigmoidal function (eqn (3)), which shows excellent agreement across the entire temperature range in both linear and logarithmic coordinates (inset), guaranteeing the accuracy of this imaging approach.

$$FIR = 0.05 + \frac{2782.5}{\left(1 + 10^{-0.012(713.3-T)}\right)} \quad (3)$$

The relative sensitivity derived from this calibration is plotted in Fig. 7(b). The maximum S_R reaches 2.9% K^{-1} at 483 K, a value that ranks highly among FIR-based thermometric materials. Crucially, the operational temperature range for imaging starts from a significantly lower temperature (333 K) compared to the previously reported SrB_4O_7: Sm^{2+} (383 K),[22] since the fitting result of $Sr_2B_5O_9Cl$: 2% Sm^{2+} are better than SrB_4O_7: Sm^{2+} at lower temperature. Therefore, it broadens the potential application scope, as many modern sensing applications require operation from near room temperature up to 500 K.

To demonstrate practical application, we performed temperature imaging on a printed circuit board (PCB) (Fig. 8). A wire on the PCB was heated by applying different electrical currents (2.5, 3.0, 3.5 A), creating a localized temperature rise and a corresponding spatial gradient. The sample powder, coated uniformly over the area of interest, translated this temperature distribution into an FIR distribution. The resulting temperature maps for different currents are displayed in Fig. 9. As anticipated, the wire location is clearly identifiable as the hottest region, with temperature decreasing with increasing distance from the wire center, effectively visualizing the thermal profile.

The above result indicates that $Sr_2B_5O_9Cl$: 2% Sm^{2+} for the TRIR method is very promising for thermal sensing applications.

Time-resolved intensity ratio imaging

The time-resolved intensity ratio technique serves as a simplification of the decay lifetime measurement to meet the demand for rapid imaging. This method involves capturing two images at different delay times (time gates, T_1 and T_2) after the

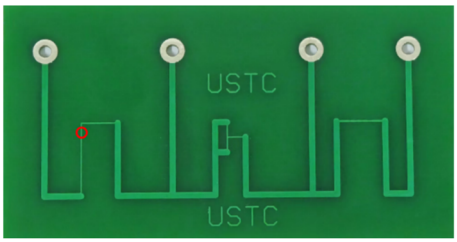

Fig. 8 The PCB used in temperature imaging study based on dual-light-path method.

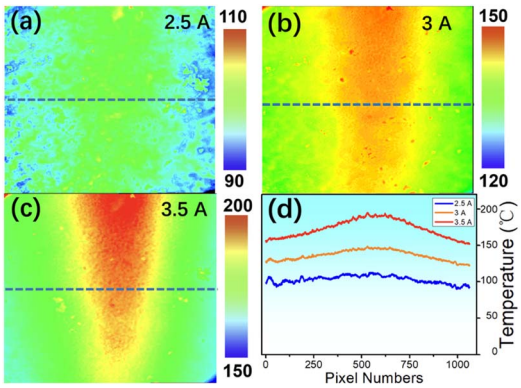

Fig. 9 Temperature distribution of the target area with currents of 2.5 A (a), 3 A (b), and 3.5 A (c); (d) the temperature distribution of the dashed line location.

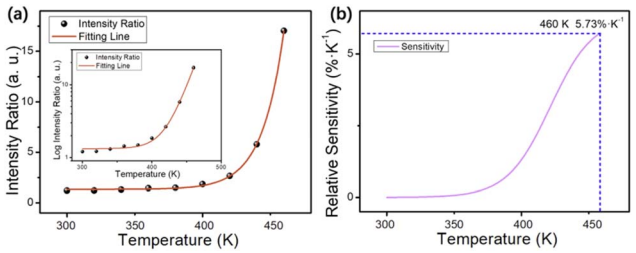

Fig. 10 (a) The fitting result of the temperature dependent time-resolving intensity ratio based on ICCD camera; (b) relative sensitivity of time-resolving intensity ratio.

excitation pulse. The choice of T_1 and T_2 is critical as it represents a trade-off between sensitivity and operational range. A larger interval between T_1 and T_2 enhances temperature sensitivity; however, if T_2 substantially exceeds the fluorescence lifetime, the fluorescence signal becomes excessively weak, thereby significantly degrading the signal-to-noise ratio. After optimization, the time gates T_1 and T_2 were set to be 0.5–1.5 ms and 15–25 ms, respectively. For calibration, the ICCD camera was used to acquire image pairs at these two time gates across a range of temperatures, and the ratio of the integrated intensities ($\mathrm{Image}_{T_1}/\mathrm{Image}_{T_2}$) was calculated.

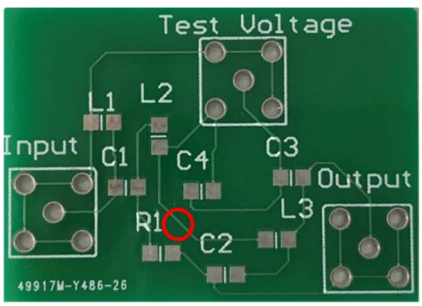

Fig. 11 The PCB used in temperature imaging study based on time-resolved intensity ratio method.

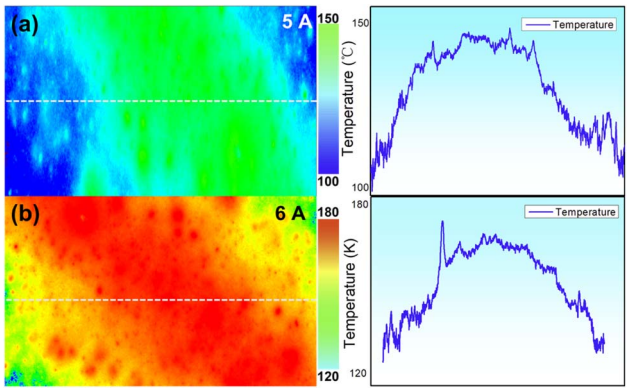

Fig. 12 Temperature distribution of the target area with currents of 5 A (a), 6 A (b). The picture at right side shows the temperature distribution of the dashed line location.

The temperature dependence of the time-resolved intensity ratio (TRIR) and its fitting curve are shown in Fig. 10(a). The data are excellently fitted by the equation:

$$\mathrm{TRIR} = 1.32 + 5.6 \times 10^{-12} e^{\frac{T}{16.04}} \quad (4)$$

The relative sensitivity for this method, calculated and plotted in Fig. 10(b), reaches a maximum of 5.73% K^{-1} at 457 K, which is higher than that achieved by the single-point lifetime measurement. Comparing with recent reported work on,[25] the DLIR and TRIR method shows relatively higher sensitivity but narrower operational temperature range.

The capability for temperature imaging was likewise demonstrated on the PCB setup (Fig. 11), using higher currents (5 A, 6 A) to generate more pronounced heating. The resulting temperature distribution maps are shown in Fig. 12. The images clearly reveal the wire as the heat source, with a temperature gradient radiating outward, and the overall temperature elevation increases with the applied current. The cross-sectional temperature profile along the dashed line quantitatively confirms this spatial thermal distribution.

Conclusions

In this work, we have successfully synthesized the $Sr_2B_5O_9Cl$: Sm^{2+} and comprehensively characterized its performance in optical thermometry and temperature imaging area. The temperature dependent behavior of FIR and Decay lifetime are obtained and the relative sensitivity is excellent. The temperature imaging using both dual light path Intensity ratio method and time resolved intensity ratio method is successfully achieved. These results indicate that $Sr_2B_5O_9Cl$: Sm^{2+} is a promising material for temperature sensing application and temperature imaging application. The high sensitivity and pronounced thermal stability of $Sr_2B_5O_9Cl$: Sm^{2+} establish it as a highly versatile and promising candidate for advanced multi-mode temperature sensing and real-time thermal mapping applications.

Author contributions

Zhongmin Cao: conceptualization, investigation, methodology, and writing – original draft. Zhicheng Liao: investigation. Qianzhang: methodology. Li Li: investigation, validation and supervision. Xianju Zhou: investigation, validation and supervision. Sha Jiang: validation. Guangxin Xie: investigation. Yonghu Chen: writing – review & editing and project administration. Min Yin: funding acquisition, writing – review & editing and project administration. Xiantao Wei: software, funding acquisition, writing – review & editing and project administration.

Conflicts of interest

There are no conflicts to declare.

Data availability

The data that support the findings of this study are available from the corresponding author upon reasonable request.

Supplementary information (SI): X-ray diffraction (XRD) patterns, photoluminescence emission spectra, and temperature- dependent luminescence imaging of the as-prepared $Sr_2B_5O_9Cl$ samples with different Sm^{2+} doping concentrations, which support the relevant conclusions presented in the main manuscript. See DOI: https://doi.org/10.1039/d5ra09629d.

Acknowledgements

This work is financially supported by National Natural Science Foundation of China (62375255, 12574445), the Science and Technology Research Program of Chongqing Municipal Education Commission (KJZD-M202300601), Natural Science Foundation of Chongqing (CSTB2025NSCQ-LZX0146), Venture and Innovation Support Program for Chongqing Overseas Returnees (CX2019085, CX2022024).

Notes and references

1 Q. Zhang, Z. C. Liao, L. T. Qiu, X. T. Wei, Y. H. Chen and M. Yin, Investigation of SrB_4O_7:Tm^{2+} luminescence for temperature imaging with high sensitivity based on time-resolved luminescence, *Dalton Trans.*, 2024, **53**, 14289–14299.

2 L. T. Qiu, Q. Zhang, Z. C. Liao, Y. H. Chen, X. T. Wei and M. Yin, The Temperature Imaging Study Based on the Time-Resolved Luminescence Measurement of Mn^{4+}-Doped $Lu_3Al_5O_{12}$ Phosphor, *Laser Photonics Rev.*, 2025, 00246.

3 L. T. Qiu, Q. Zhang, Z. C. Liao, F. F. Chi, Y. H. Chen, X. T. Wei and M. Yin, High-quality temperature imaging of Li_2TiO_3:Mn^{4+} thin film based on time-resolved luminescence measurement, *J. Alloys Compd.*, 2024, **1008**, 176543.

4 Z. M. Cao, X. T. Wei, X. J. Zhou, L. Li, Y. H. Chen, Y. J. Wang, G. X. Xie and M. Yin, Thermal imaging study of Sm^{2+} doped SrB_4O_7 based on time-resolved technology, *Dalton Trans.*, 2023, **53**, 285–291.

5 Y. Kuang, D. Yang, S. Gai, F. He, B. An and P. Yang, Uncovering Different Responses and Energy Mechanisms of Sensitizer and Activator in Host Manipulation for Upconversion Nanoparticles, *Inorg. Chem.*, 2023, **62**, 10805–10821.

6 Y. Kuang, T. Li, T. Jia, A. Gulzar, C. Zhong, S. Gai, F. He, P. Yang and J. Lin, Insight into the Luminescence Alternation of Sub-30 nm Upconversion Nanoparticles with a Small $NaHoF_4$ Core and Multi-Gd^{3+}/Yb^{3+} Coexisting Shells, *Small*, 2020, **16**, 2003799.

7 J. Xu, R. Shi, G. Chen, S. Dong, P. Yang, Z. Zhang, N. Niu, S. Gai, F. He, Y. Fu and J. Lin, All-in-One Theranostic Nanomedicine with Ultrabright Second Near-Infrared Emission for Tumor-Modulated Bioimaging and Chemodynamic/Photodynamic Therapy, *ACS Nano*, 2020, **14**, 9613–9625.

8 W. Zhou, Thermally coupled energy levels of rare-earth Er-based nanomaterials for high-precision and reliable temperature sensing, *J. Alloy. Compd.*, 2025, **1022**, 179919.

9 Z. Ju, Y. Shi, F. Meng, J. Huang, W. He and R. Lv, High-Sensitivity Optoelectronic Temperature Sensing Using Rare Earth Luminescent Materials for Antenna Radome Temperature Monitoring, *ACS Appl. Mater. Interfaces*, 2025, **11**, 40729–40742.

10 R. Wu, C. Xu, J. Zhang, E. Huang, K. Ding, H. Sun and L. Xu, Thermally stable white light emission and thermometer in rare earth doped lithium niobate micro-crystals synthesized *via* the soluble method, *Ceram. Int.*, 2025, **51**, 18731–18739.

11 Y. Chen, F. Qin, W. Zhang, Q. Dong, Z. Yang and G. Bai, Achieving high-sensitivity optical temperature sensing and anti-counterfeiting based on rare earth ions-doped $SrLaLiTeO_6$ phosphors, *Ceram. Int.*, 2025, **51**, 36247–36254.

12 W. M. Piotrowski, K. Kniec-Stec, M. Suta, B. Bogielski, B. Pozniak and L. Marciniak, Positive luminescence thermal coefficient of Mn^{2+} ions for highly sensitive luminescence thermometry, *Chem. Eng. J.*, 2023, **464**, 142492.

13 C. Zhang, H. Tang, J. Li, Q. Song, X. Li, X. Cao, C. Zhang, F. Wu, B. Liu and J. Xu, Boltzmann thermometer with broadband emission in Mn^{4+}-Doped β-Ga_2O_3 crystals, *J. Lumin.*, 2024, **267**, 120334.

14 B. Zhu, L. Wang, Q. Shi, H. Guo, J. Qiao, C. Cui and P. Huang, $MgGa_2O_4$:Mn^{2+}, Mn^{4+}: A dual-emitting phosphors with unique optical temperature sensing, *J. Alloy. Compd.*, 2023, **948**, 169717.

15 Y. Kato, Y. Shimazaki, S. Chuma, K. Shiraya, Y. Nakane, T. Sugi, K. Okabe, Y. Harada and S. Sotoma, Fluorescent Thermometers Based on Carbon Quantum Dots with Various Detection Modes for Intracellular Temperature Measurement, *Nano Lett.*, 2025, **25**, 5688–5696.

16 Y. Zhu, J. Buitenhuis, B. Förster, M. Vetrano and E. Koos, Development of Perovskite Quantum Dots for Two-Dimensional Temperature Sensors, *ACS Appl. Nano Mater.*, 2023, **6**, 4661–4671.

17 Q. Liu, M. Wu, B. Chen, X. Huang, M. Liu, Y. Liu, K. Su and X. Min, Optical thermometry based on fluorescence intensity

ratio of Dy^{3+}-Doped oxysilicate apatite warm white phosphor, *Ceram. Int.*, 2023, **49**, 4971–4978.

18 F. Hu, S. Ren, Y. Wu, C. Sun, B. Zhu, Q. Wang, S. Li and D. Zhang, Dual-mode optical thermometer based on fluorescence intensity ratio of Eu^{3+}/Mn^{4+} co-doping zinc titanate phosphors, *Spectrochim. Acta, Part A*, 2023, **288**, 122127.

19 Z. Cao, X. Wei, L. Zhao, Y. Chen and M. Yin, Investigation of SrB_4O_7:Sm2+ as a Multimode Temperature Sensor with High Sensitivity, *ACS Appl. Mater. Interfaces*, 2016, **8**, 34546–34551.

20 W. Piotrowski, Sensitization of Ti^{3+} Persistent Luminescent Lifetime-Based Thermometer by Ln^{3+} Co-Doping, *J. Phys. Chem. C*, 2025, **129**, 3067–3075.

21 L. Wu, M. Jia, D. Li and G. Chen, Shell Engineering on Thermal Sensitivity of Lifetime-Based NIR Nanothermometers for Accurate Temperature Measurement in Murine Internal Liver Organ, *Nano Lett.*, 2023, **23**, 2862–2869.

22 J. Xiong, M. Zhao, X. Han, Z. Cao, X. Wei, Y. Chen, C. Duan and M. Yin, Real-time micro-scale temperature imaging at low cost based on fluorescent intensity ratio, *Sci. Rep.*, 2017, **7**, 41311.

23 Q. Zeng, N. Kilah, M. Riley and H. Riesen, Luminescence properties of Sm^{2+}-activated barium chloroborates, *J. Lumin.*, 2003, **104**, 65–76.

24 P. Plachinda、V Dolgikh、S Stefanovich and P. Berdonosov, Nonlinear-optical susceptibility of hilgardite-like borates $M_2B_5O_9X$ (M = Pb, Ca, Sr, Ba; X = Cl, Br), *Solid State Sci.*, 2005, **7**, 1194–1200.

25 L. Cui, Z. Dong, D. Yu, Y. Wang and A. Meijerink, High-sensitivity luminescent temperature sensors: MFX:1%Sm^{2+} (M = Sr, Ba, X = Cl, Br), *Sci. Adv.*, 2024, **10**, 7737.

26 M. Dai, Y. Li, Z. Wang, A. Li, T. Sheng, H. Xu, K. Li and Z. Fu, Thermally boosted upconversion luminescence and high-performance thermometry in ScF_3:Yb^{3+}/Tm^{3+} nanorods with negative thermal expansion, *J. Lumin.*, 2023, **265**, 120219.

27 E. Ilya, V. M. Daria, A. K. Mikhail, A. K. Mikhail, A. M. Vassily, Y. K. Evgenii and A. M. Alina, Single *vs.* mutliparametric luminescence thermometry: the case of Eu^{3+}-doped $Ba_3(VO_4)_2$ nanophosphors, *J. Mater. Chem. C*, 2023, **11**, 14814.